Article

Magnetically-Driven Reconfigurable Cilium Array with Tunable Wettability for Dynamic Display and Controllable Microreaction

Zijing Quan [1], Yuhan Zhang [1,*], You Pan [1], Zhongyi Yang [1], You Chen [1], Fawei Rui [1], Letian Li [1], Bo Li [1,2,*], Shichao Niu [1,2,3,*], Zhiwu Han [1,2,3], and Luquan Ren [1,2,3]

[1] Key Laboratory of Bionic Engineering (Ministry of Education), Jilin University, Changchun 130022, China
[2] National Key Laboratory of Automotive Chassis Integration and Bionics, Jilin University, Changchun 130022, China
[3] Institute of Structured and Architected Materials, Liaoning Academy of Materials, Shenyang 110167, China
* Correspondence: yhzhang9922@mails.jlu.edu.cn (Y.Z.); boli@jlu.edu.cn (B.L.); niushichao@jlu.edu.cn (S.N.)
Received: 3 March 2025; Revised: 17 March 2025; Accepted: 25 March 2025; Published: 28 March 2025

Abstract: Efficient droplet transport plays an important role in many fields such as liquid collection, microfluidic management, and reaction control. However, it remains a key challenge to achieve fast and precise droplet motion control along a predetermined path. Herein, a magnetically driven cilium array (MDCA) was developed by a simple one-step spraying method. The MDCA exhibits both upright and prostrated states under a programmable magnetic field, achieving in-situ pinning and driving of the droplets, respectively. In particular, the MDCA modified by the silicone oil can not only be used for precise droplet manipulation on the spatio-temporal scale (S-shaped trajectory transport, selective control of target droplets, and velocity control) but also provides a self-enclosed space for droplet fusion for chemical microreactions, allowing fine-tuning of reaction parameters and isolation from external contamination. Based on the theoretical analysis of droplet transport, MDCA can be applied to the development of dynamic digital displays and chemical microreactors and provides inspiration for the development of environmental monitoring, drug delivery, and energy purification.

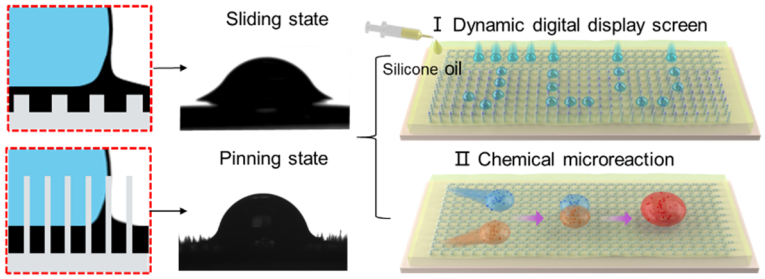

Keywords: magnetically driven; cilium array; tunable wettability; droplet motion control

1. Introduction

Dynamic programmable regulation of droplet motion [1,2] is of great scientific importance and application value in the fields of droplet transport [3], reaction control, environmental monitoring [4], 3D printing [5–8] and biomedicine [9,10]. However, it is difficult for conventional droplet regulation methods to achieve effective switching between in-situ pinning and fast sliding of droplets on a single surface, limiting their application in complex motion path scenarios [11,12]. Therefore, it remains a key challenge to achieve fast and precise motion manipulation of droplets along a programmable path through simplified design.

To improve droplet controllability [13], researchers have attempted to achieve controllable liquid dynamics through the design of material surface energy gradients [14–16] and the construction of hierarchical micro-nanostructures [17,18], aided by external fields such as heat [19], light [20,21], acoustic [22], electric [23,24], and magnetic fields [16,25,26]. In particular, magnetic drive offers unique advantages, including non-contact real-time control, fast response, and no specific environmental requirements. The design principles can be summarised in two different categories: (1) Direct actuation [27] of droplets by adding magnetic particles directly to the droplet [28]; (2) Indirect actuation of droplets by deforming the magnetic particle assemblies wrapped in flexible membranes in response to the magnetic field [29–31]. However, the direct addition of magnetic particles to a droplet limits the types of droplets that can be driven. Meanwhile, the deposition of magnetic particles tends to deteriorate

the driveability. On the contrary, for the typical indirect liquid manipulation method driven by an external magnetic field, the magnetic cilia [32] produce a directional motion [33–35] that enables the control of the liquid's directional rolling. This technique provides controlled directional transport of liquids while also demonstrating adaptability to different droplet actuation and magnetic field conditions, making it a promising solution for microfluidic [30], biomedical engineering, and environmental monitoring applications. However, conventional magnetically controlled cilia exhibit limitation: The inertial rolling of droplets on cilia makes tuning of the adhesion properties [36,37] difficult, affecting the precision of programmable pathway transport of droplets.

In this work, a magnetically driven cilium array (MDCA) was developed by a simple one-step spraying method. The MDCA achieves fast switching between two states (upright and prostrated) driven by a magnetic field, leading to pinning and sliding behaviours of droplets, respectively. This design not only simplifies the preparation process but also significantly improves the flexibility of droplet manipulation. To further optimise the droplet motion performance, silicone oil [38,39] was used for surface modification of MDCA. The silicone oil formed spontaneously a closed environment at the periphery of the droplet, which created a smooth start-up of MDCA when it switched from the upright state to the prostrated state, thus overcoming the detrimental effect of inertia on the accuracy of droplet manipulation. The SOMDCA reduces the impact of natural cilia defects on droplet driving. Specifically, silicone oil-modified MDCA (SOMDCA) was capable of driving droplets in programmable pathways (inversed S-shape motion, in-situ selective drive of the target droplet, and velocity control) based on droplet static thermodynamic mechanism and dynamic slippage principle. In addition, the proposed optimal SOMDCA is critical for the design of digital display screens and chemical microreactors that isolate the outside environment. This superwettable surface provides new research ideas and technical guidance for the development of magnetic fluid manipulation technology, environmental monitoring, microfluidic chips and biomedicine.

2. Methodology

2.1. Fabrication of the MDCA

To fabricate the MDCA, a 4 cm × 4 cm neodymium magnet (~0.5 T), an airbrush, and polyethylene terephthalate (PET) substrates were prepared. The PET substrate was fixed at a 6 mm precise distance above the magnet to ensure the vertical alignment of the magnetic particles encased in liquid during the spraying process. The detailed fabrication procedure is described as follows: The precursor solution was prepared by adding 2.4 g polydimethylsiloxane (PDMS), 0.17 g curing agent and 2.4 g carbonyl iron powder (CIP, 5 μm in diameter) to 5 g ethyl acetate (EA). The solution was thoroughly stirred with a glass rod for 30 min to ensure uniform dispersion of CIPs within the PDMS and EA matrix. The prepared solution was then transferred into an airbrush, maintaining PDMS in a 30 cm distance between the airbrush nozzle and the PET substrate (Figure 1a), which is to ensure that the magnetic particles encased in liquid were evenly deposited parallel to the substrate surface. The spraying process was conducted for 50 s, after which the magnet and coated PET substrate were immediately placed in an oven and dried at 60 °C for 5 h. This process resulted in the successful fabrication of the MDCA surface.

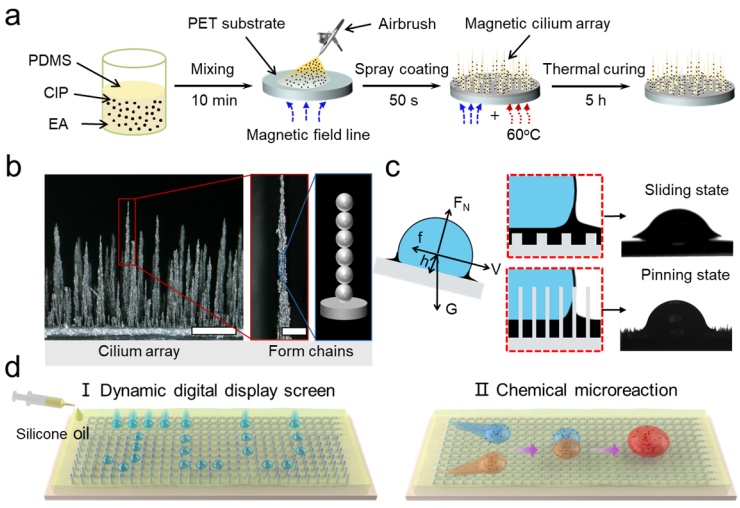

Figure 1. Dynamically reconfigurable SOMDCA design and working Principle. (**a**) Preparation diagram of MDCA. (**b**) Optical UDFM images of MDCA. The interpolated scales are 500 μm and 100 μm respectively. (**c**) Mechanical force analysis of droplets and schematic diagrams illustrating the mechanisms of the sliding and pinning states. (**d**) Applications of SOMDCA surface (**I**: Dynamic digital display screen; **II**: Chemical microreaction).

2.2. Droplet Adhesion Property on SOMDCA

The centrifugation was utilized to measure the maximum adhesion strength of a 10 μL droplet on the MDCA surface which was modified with silicone oils of varying viscosities, in an upright state. The experimental procedure was as follows: the SOMDCA was placed directly above the magnet to maintain the cilia in an upright orientation. This combination was placed at a radial distance of R from the rotation center. By systematically varying the rotational velocity and employing an external camera to capture the instant of droplet detachment, the adhesion strength of the droplet under the influence of silicone oils with different viscosities was evaluated. The adhesive force of the droplet on the SOMDCA was calculated using the equations $\omega = 2\pi n/60$ and $F = m\omega^2 R$, where ω represents the angular velocity, n is the rotational velocity, m is the mass of the droplet, and R is the radial distance from the rotation center.

2.3. Chemical Microreaction

The droplets of $FeCl_3 \cdot 6H_2O$ and KSCN were prepared at a concentration of 1 M and 3 M each. The chemical equation is as follows: $Fe^{3+} + 3SCN^- = Fe(SCN)_3$. The temperature of the chemical reaction was measured using a thermal imager (Hti HT-18, made in Zhejiang, China). Gaussian 16 is used to measure molecular energy values before and after chemical reactions. The red droplets (10 μL) are consist of a mixture of carminic acid and water at a weight ratio of 1:50.

2.4. Characterization

The morphological characteristics of the MDCA were characterized using the Ultra-deep Field Microscope (UDFM, Keyence VHX-6000, made in Osaka, Japan) and Laser Scanning Confocal Microscope (LSCM, Zeiss LSM 980, made in Oberkochen, Germany). The water contact angle and sliding angle were obtained by a contact angle measurement system (Sindin SDC-100, made in Shenzhen, China). Magnetic force simulation tests of magnets were conducted by Comsol 6.0.

3. Results and Discussion

3.1. Design and Working Principle of Dynamically Reconfigurable SOMDCA

To achieve stable droplet pinning and sliding behaviors, a surface capable of rapid switching between two states (upright and prostrated state) under magnetic actuation has been developed. In this work, a simple spray-coating method was employed, leveraging the unique magnetic responsiveness of magnetic particles. By systematically adjusting the ratios of PDMS, CIP, and EA, the formulation with high spray-coating uniformity was optimized. The detailed preparation method has been comprehensively described in the experimental section, as illustrated in Figure 1a. Specifically, the magnetic particles produce a magnetic force in the presence of a magnetic field. As the system tends to reach its minimum energy state, the magnetic dipole interactions between the particles cause them to align into chain-like structures within the magnetic field. This ordered arrangement of particles in the magnetic field reduces the system's magnetic energy, thereby promoting CIPs upward growth. The magnetic moment of CIPs can be described by the following formula: $M = \chi H$. M is the magnetization (A/m), χ is the magnetic susceptibility of the CIPs, and H is the applied magnetic field strength (A/m). The growth direction is determined by the magnetic field gradient and the magnetic moment of the particles. After the PDMS encapsulating the magnetic particles has been cured, the magnetic particles maintain an upright configuration even in the absence of an applied magnetic field. Figure 1b presents the topographic characteristic of the MDCA under UDFM, revealing that the magnified single magnetic cilium exhibits a stacked growth pattern of magnetic particles to minimize energy.

After the surface modification of the MDCA with silicone oil, the force analysis of droplets, as well as the mechanisms underlying the pinned and sliding states, along with their contact angles respectively, were further investigated (Figure 1c). Due to the low surface energy (21.2 mN/m, 1000 cP) of silicone oil, when the droplet was deposited on the superwetting surface of the prostrated cilium array, the silicone oil may spread and "mask" the droplet. As the silicone oil infiltrates and submerges the microstructure surface, the SOMDCA exhibits an extremely low roll-off angle, with negligible contact line pinning. In this case, the total interfacial energy per unit area: $E = \gamma_{ow} + r\gamma_{os}$. Where γ is the interfacial tension between the two phases designated by subscripts water (w), oil (o), and air (a). And r is the ratio of the total surface area to the projected area of the solid. Different from the prostrated state, when a droplet resides on a superwetting surface with upright cilia, despite the droplet's tendency to slide forward due to gravitational force, the array of upright cilia with a high aspect ratio obstructs the

droplet's sliding progression, macroscopically manifesting as a pinned state. On this basis, dynamically reconfigurable MDCA can achieve the switching between the pinning and sliding states of droplets under the actuation of a magnetic field thereby enhancing the programmed design and precise control of droplets. Specifically, by utilizing the surfaces with super wettability, a new generation of digital dynamic display screens and chemical microreactors (Figure 1d) was designed. These innovations hold promising prospects for various fields, including magnetic fluid manipulation technology, environmental monitoring, drug delivery, and energy purification.

3.2. Characterization and Optimization of MDCA

To further optimize the driving performance, the MDCAs and the magnetically controlled properties were characterized and refined. Six kinds of MDCAs were prepared based on varying contents of PDMS and CIP. Specifically, three grades (high (H), middle (M), and low (L)) were set for both PDMS and CIP content. The first letter of the abbreviation is PDMS content and the last letter is CIP content. Detailed content information is provided in Table S1. Utilizing UDFM, an investigation was conducted into the height, magnetic compliance, and uniformity of MDCA distribution fabricated using various contents (Figure 1b). As illustrated in Figure 2a, the cilia comply with the magnetic field direction, regardless of whether the magnetic field is designed to be orientated perpendicular or parallel to the substrate. The magnetic cilia compliance to the magnetic field is shown in Figure S1. The growth and alignment of MDCA are significantly influenced by the PDMS and CIP concentrations in the solution, as well as the strength of the external magnetic field. Based on the experimental results and relevant theories, the following analysis is conducted. The viscosity η of the PDMS solution can be described by the equation: $\eta = \tau/\gamma$. Where η is solution viscosity (Pa·s), τ is the shear stress (Pa), γ is the shear rate (1/s). Specifically, PDMS serves as the structural matrix of the cilium array, providing flexibility and strength. The PDMS concentration has a substantial impact on the solution viscosity, which in turn affects the spraying process and the subsequent cilia morphology. For sample LM with lower PDMS concentrations, the solution exhibits reduced viscosity, leading to a more uniform spray pattern and the formation of taller cilia. However, this lower viscosity also results in weaker adhesion between the cilia and substrate, causing an increased propensity for cilia detachment (Figure S2b). As the concentration of PDMS increases in sample HH, the solution becomes more viscous, which can hinder the uniform distribution of particles during the spraying process leading to a decrease in cilia height (Figure S2c). Higher viscosity results in poorer particle dispersion, as predicted by the particle deposition model. Thus, an excessive PDMS concentration leads to a reduction in cilia height due to non-uniform particle distribution during the spraying process.

The magnetic responsiveness of cilia is attributed to CIPs. The concentration of CIPs directly influences the magnetic alignment of cilia in an external magnetic field. At lower CIP concentrations, the limited number of magnetic particles tends to adhere more closely to the substrate, resulting in shorter cilia growth heights. At higher CIP concentrations of the sample MH, the enhanced magnetic responsiveness leads to increased interparticle interactions, potentially causing agglomeration and uneven particle distribution. This effect, commonly referred to as magnetic agglomeration, results in higher average cilium heights but reduced uniformity. At moderate CIP concentrations of sample MM, the cilia effectively align under the magnetic field, leading to uniform growth and optimal height. The magnetic field facilitates the directional alignment of CIPs, promoting uniform self-assembly of cilia. The sample MM exhibits the most uniform cilium distribution and optimal magnetic compliance.

Subsequently, LSCM was employed to conduct an in-depth investigation into the morphological characteristics and distribution patterns of cilia (Figure 2b). This process successfully obtained height simulation distribution maps of magnetic cilium arrays in both upright and prostrated states, agreeing with the results obtained by UDFM. A detailed quantitative analysis using Abbott curve simulations was further conducted on the cross-sectional area fractions of the MDCA (Figure 2c–e). Figure 2c illustrates the trend of cross-sectional area fraction varying with height in the upright state. Specifically, the highest cross-sectional occupancy is gradually increasing, possibly due to the increasing diameter and height of the cilia with increasing CIP concentration, which is consistent with the results of previous analyses. Notably, PDMS and CIP at middle concentrations exhibit dual peak cross-sectional areas, suggesting probably the presence of two types of cilia: tall cilia and short cilia. This situation not only increases the retention capacity of silicone oil on the surface of the cilia but also reduces the height of the cilia in the prostrated state and decreases the surface roughness. In contrast, the simulation results for the samples LL and MM do not reflect the presence of these two types of cilia. Similarly, Figure 2d demonstrates the variation of cross-sectional area fraction changing with height in the prostrated state. With the increase in CIP concentration, the prostrated cilia height also increases. Notably, the sample MM exhibits a more marked prostrated effect, which may be attributed to the dual height peaks of cilia in Figure 2c. Ultimately, based on the

analysis in Figure 2e, the samples MM in the prostrated state have the highest percentage of cross-sectional integration, which suggests a certain degree of homogeneity of the cilia, a property that positively affects droplet sliding.

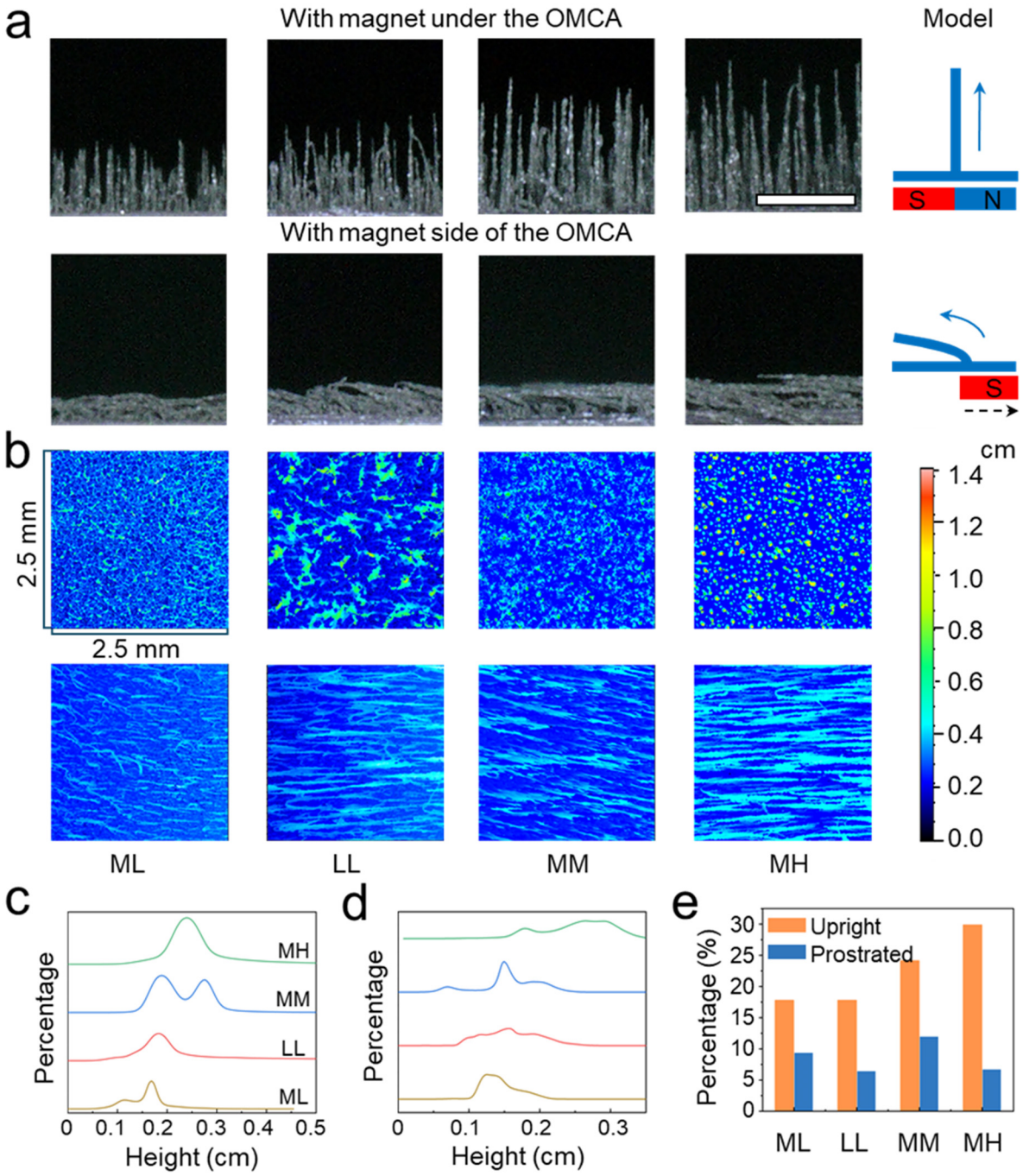

Figure 2. Characterization and optimization of MDCA. (**a**) UDFM images of the upright and prostrated MDCA. The interpolated scale is 1 cm. (**b**) LSCM images of the upright and prostrated MDCA. Cross-section proportion of (**c**) upright and (**d**) prostrated. (**e**) Cross-section proportion diagram of four kinds of MDCAs.

3.3. Magnetically Driven Droplet Transport Performance and Optimization

To demonstrate that the prepared SOMDCA surface possesses tunable droplet adhesion, a centrifuge was utilized to characterize the adhesion force of droplets on the SOMDCA surface with varying viscosities, based on the action of centrifugal force, as shown in Figure 3a.

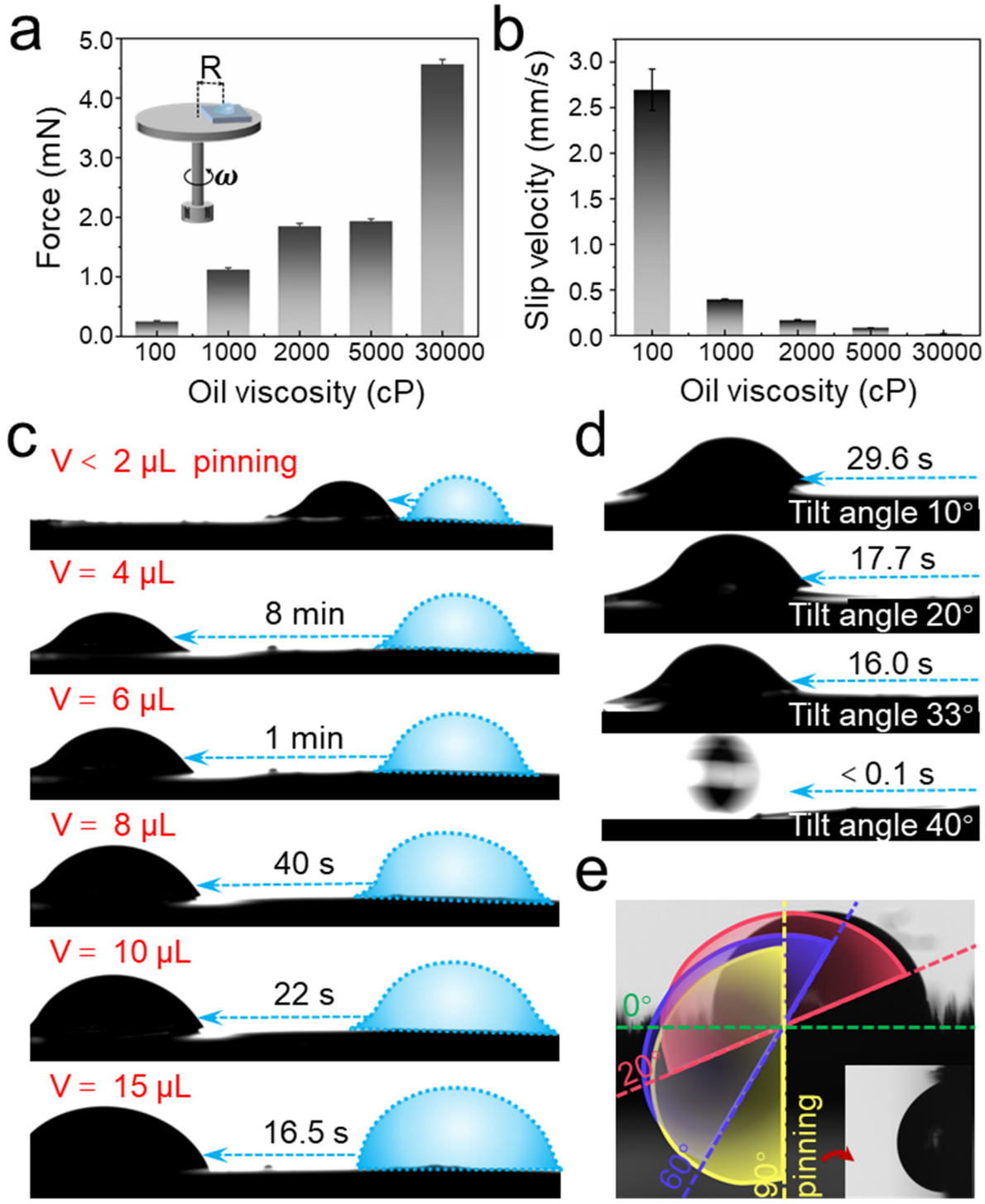

Figure 3. Optimization of magnetically driven droplet transport performance. (**a**) The critical adhesion of droplet adhesion on SOMDCA surface under different viscosity of silicone oils. (**b**) The sliding velocity of 10 μm droplet under different viscosity of silicone oils. (**c**) Effect of volume on droplet sliding ability. (**d**) The sliding ability of droplets at different obliquity angles of SOMDCA surface. (**e**) The droplet pinning state diagram of at different angles of SOMDCA surface.

The experimental results indicate that after placing a cylindrical permanent magnet beneath the SOMDCA surface, the pinning force of droplets on the SOMDCA surface increased with the viscosity of the silicone oil. The adhesion force of the silicone oil with a viscosity of 1000 cP on the SOMDCA surface reached 1.2 mN, which is 12 times the mass of the droplet itself. Subsequently, MDCA surfaces were modified with silicone oils of different viscosities, which significantly influenced the sliding velocity of the droplets (Figure 3b). As the viscosity of the silicone oil increased, the droplet sliding velocity changed from 0.019 mm/s to 2.7 mm/s, which illustrates the high viscosity of silicone oil significantly reducing droplet mobility. At a 30,000 cP viscosity, droplet movement on the SOMDCA surface was negligible. An appropriate droplet viscosity should enable control over droplet pinning and

precise manipulation of droplet movement under fast sliding conditions. The SOMDCA with a viscosity of 100 cP exhibited excessively fast sliding velocities, making it difficult to precisely control the motion trajectory of the droplets, while those with viscosities above 2000 cP resulted in excessively slow droplet sliding, neither of which were considered to possess excellent precision control over droplet movement. Therefore, silicone oil with a viscosity of 1000 cP was selected for subsequent droplet manipulation experiments. Although droplets can also be driven at 0°, the velocity is too slow (Figure S7). To demonstrate the superior droplet control performance of the prepared SOMDCA surface, the sliding capability of droplets with varying volumes was explored on the SOMDCA in a prostrated state at a 10° tilt angle. The driving magnets effect model for droplets on SOMDCA is shown in Figure S3. As shown in Figure 3c, a 2 μL droplet, even on the prostrated SOMDCA surface, only slid a short distance before pinning to the surface. This is because when the droplet falls onto the surface, its gravitational potential energy is partially converted into kinetic energy, causing a brief sliding phenomenon. After this energy is expended, the droplet, with insufficient gravitational force, cannot overcome the resistance of the higher parts of the prostrated cilia, resulting in complete pinning on the surface. Secondly, when the droplet volume reached 4 μL, the droplet exhibited sliding capability on the surface, but the sliding velocity was relatively slow, taking approximately 8 min to cover a distance of 10 mm. When the droplet volume reached 15 μL, the sliding velocity (0.61 mm/s) significantly increased, being 29 times that of the 4 μL droplet. Additionally, the sliding capability of the droplets varied at different tilt angles, as shown in Figure 3d. The greater the tilt angle, the faster the sliding velocity of the droplets. At a 40° tilt angle, the droplets could roll rapidly off the surface, instead of being pinned or sliding on the SOMDCA surface for silicone oil struggling to capture droplets with an excessively large gravitational potential energy component. In contrast, when the magnetic field causes the cilia to stand upright, a 10 μL droplet remains firmly fixed on the surface even as the SOMDCA is tilted from 0° to 90° (Figure 3e), which is different from sample LL for droplet sliding off the upright SOMDCA surface with a 10° tilt angle (Figure S4 and Video S1). This observation underscores the robust adhesion and stability of the SOMDCA over the droplet under the influence of the magnetic field, highlighting the effective control over droplet immobilization achieved through the upright cilia configuration. To ensure controlled droplet movement, a 10° inclination was selected for subsequent experiments.

3.4. Droplet Programmed Manipulation

Utilizing the gravitational force of droplets to facilitate their sliding or pinning on inclined surfaces represents a traditional methodology. Nonetheless, the challenge of achieving controllable regulation of droplet pinning and sliding in situ is not easily surmounted through mere material and structural design. Intriguingly, magnetically actuated droplet sliding emerges as a microfluidic technology underpinned by magnetic field modulation, which enables rapidly dynamic regulation with minimal energy expenditure. By judiciously designing the magnetic field distribution and changing surface characteristics, it is feasible to effectuate in situ toggling between sliding and pinning of droplets on inclined surfaces. However, this technique typically confines droplet propulsion to the direction dictated by gravity, thereby presenting challenges for precise manipulation and the customization of droplet trajectories. This research employs magnets to customize droplet sliding paths by modulating droplet slippage and pinning, demonstrating significant advantages in the field of micro-droplet manipulation.

During the experiment, the SOMDCA surface was tilted at 10°, and the droplet moved along a predetermined inverted S-shaped trajectory under the influence of a magnetic field. The superwetting surface properties changed with the magnetic field gradient, enabling the droplet to overcome the effects of gravity and slide precisely along the inverted S-shaped path. This method not only exceeds the limitations of traditional droplet sliding, which relies solely on gravity for directional movement, but also the ability of SOMDCA to switch between in-situ anchoring and sliding provides new possibilities for precise droplet control on complex paths. As shown in Figure 4a and Video S2, the droplet exhibited an inverted S-shaped curved slide under the driving action of two small magnets. To detail the driving method and principle of this path, a simulation of two small magnets (N35) was conducted using Comsol. Combining finite element analysis, the spatial distribution of the magnetic field, as well as the direction and intensity of their magnetization vectors, were obtained by solving Maxwell's equations (Figure 4e). During the preparation of MDCA, the magnetic particles were influenced by the magnetic field, causing the magnetic poles to align directionally. This alignment allows the cilia to bend towards the direction of the magnetic field lines under the influence of an external magnetic field, overcoming their inherent elastic force. According to the distribution characteristics of the magnetic field, the magnetic cilia above the two magnets stand upright, while those between the two magnets collapse. Therefore, by continuously adjusting the position of the magnets, the droplet is positioned between 1.5 mm magnets, allowing the droplet's sliding path to be altered, thus enabling the droplet to slide along the predetermined inverted S-shaped path. Similarly, using the magnet shown in Figure 4b,e2 and Video S3 demonstrate

the droplet's ability to slide along a programmed path at an inclination of 30°, and Figure 4c and Video S4 show the ability to switch between selective in-situ pinning and droplet sliding for two droplets. Additionally, the sliding velocity of the droplet can be controlled based on the distance between the magnet and the droplet (Figure 4d,f and Video S5). This phenomenon arises because the closer the droplet is to the magnet, the greater the compliance of the cilia, resulting in reduced surface roughness and consequently lower resistance to droplet sliding. Conversely, when the magnet is farther from the droplet, the magnetic force struggles to overcome the inherent elastic force of PDMS, resulting in greater surface roughness, which limits the droplet's sliding velocity. In comparison, silicone oil with a viscosity of 100 cP cannot achieve precise droplet control solely through gravitational force. However, with an appropriate 3D printing platform (Figure S5), it is possible to facilitate the C-shaped and S-shaped motions (Figure S6) sliding of droplets by adjusting platform tilt angle.

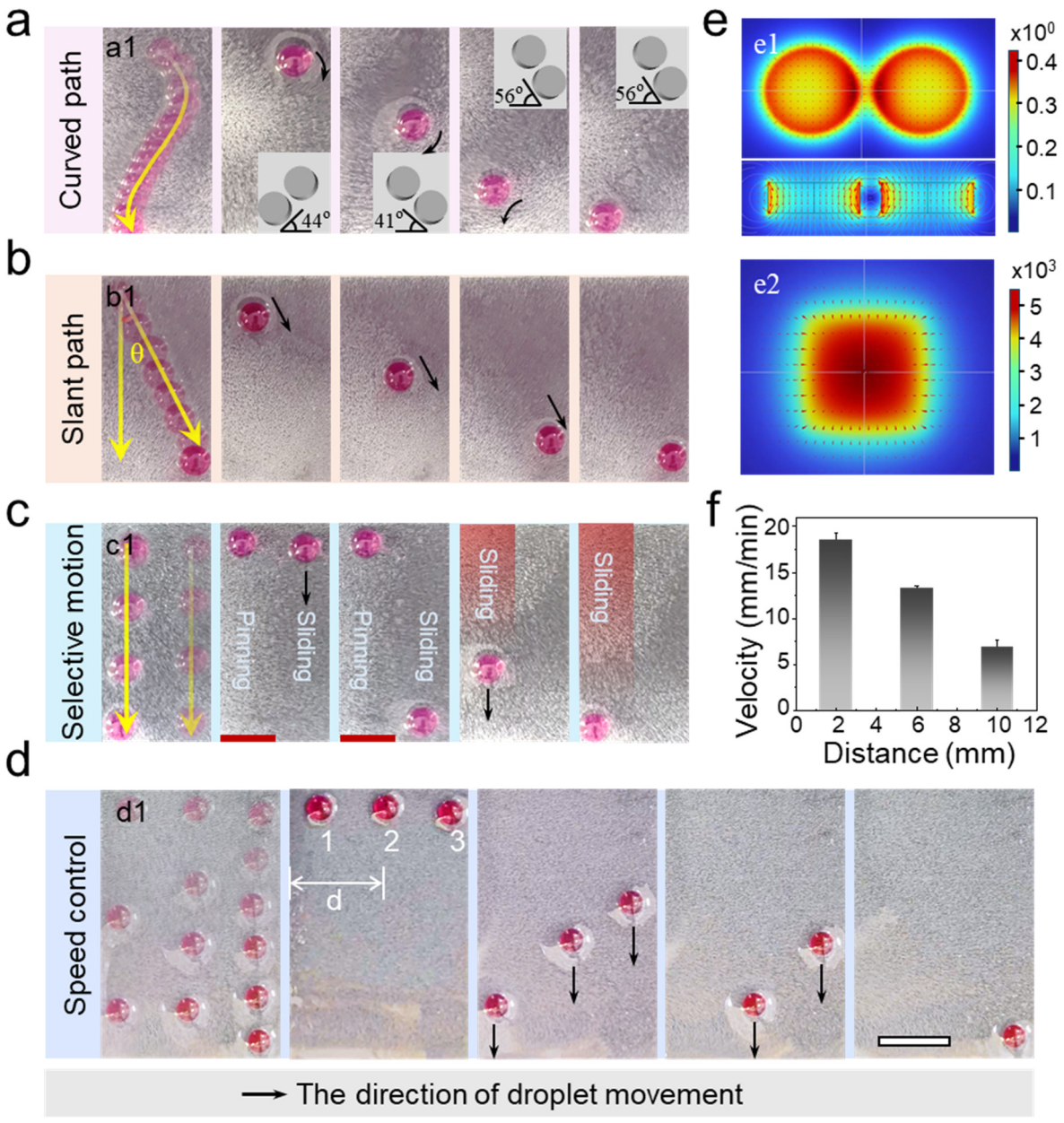

Figure 4. The precise control and path programmability by SOMDCA over droplets. (**a**) The magnet guides the droplet through the inverted S shape. (**b**) The magnet guides the droplet through the 30° inclination. (**c**) Selective pinning and sliding of droplets. (**d**) Effect picture of distance between magnet and droplet on droplet sliding velocity. (**e**) Magnetic line distribution of double round magnet and square magnet. The unit is Gs. (**f**) Effect of distance between magnet and droplet on droplet sliding velocity. The interpolated scale bars of all pictures are 2 cm.

3.5. Application Demonstration of the SOMDCA

Based on the aforementioned principles and phenomena of droplet programmed manipulation, the magnetic field-regulated microfluidic control technology demonstrates broad application prospects in multiple fields due to its non-contact nature, high precision, and programmable characteristics.

In this work, by controlling the pinning and sliding of droplets on the SOMDCA surface, dynamic digital display functionality and the driving of droplet coalescence for chemical microreactions can be achieved. Specifically, the number and position of droplets along the x-axis are pre-designed and allocated to the upright cilia at the top of the sample. Subsequently, the droplets are allowed to slide under the influence of gravity from the prostrated SOMDCA surface to the pre-designed positions, where they are anchored by the upright SOMDCA surface. This process is then repeated multiple times to stack the droplets layer by layer along the y-axis, akin to building blocks, until the formation of the letters "JLU" is achieved (Figure 5a and Video S6). Based on the standard deviation of the path, the deviations of the x-axis and y-axis are $\sigma_x = 1.2\%$ mm^2 and $\sigma_y = 2.3\%$ mm^2 respectively (Table S2). The specific locations of the letters "JLU" are illustrated in Figure 5b. Notably, based on the influence of SOMDCA on the sliding velocity of droplets with varying sizes and distances, more sophisticated dynamic patterns could be engineered in future designs to address more stringent requirements. This capability of dynamic droplets to perform digital stacking, with each droplet acting as a new unit sliding along a pre-designed path, provides novel insights for the design of next-generation dynamic digital displays.

Precision manipulation of droplets exhibits significant applications not only in dynamic digital displays but also in various areas such as droplet fusion, chemical microreactions in a self-enclosed environment, and reducing energy loss rate (Figure 5c and Video S7). Typically, in a silicone oil-enclosed environment, the fusion process of two droplets involves overcoming their surface tension and regulating interfacial dynamics. When magnetically driven to gradually approach each other, a sudden rapid movement towards each other occurs between the droplets, which is attributed to the attractive force between molecules, prompting the two droplets coated with oil to approach each other. Subsequently, as the droplets approach, the silicone oil film between them gradually thins. When the film thickness reaches a critical value (typically at the nanoscale), the film becomes unstable and ruptures. Mechanisms leading to film rupture encompass van der Waals forces, thermal fluctuations, or external perturbations. Upon film rupture, direct contact between the droplets results in a reduction in interfacial energy, thereby driving the fusion process. A chemical reaction occurs between 1 M Fe^{3+} and 3 M SCN^{-}, resulting in the transformation of the droplets from pale yellow and colorless to a blood-red color, accompanied by the generation of energy. Furthermore, Figure 5d demonstrates energy generation by employing the density functional theory method within the Gaussian 16 to conduct energy simulations before and after the reaction, as well as experiments on heat loss rates in a self-contained environment in Figure 5e. Theoretical calculations indicate that the sum of the energies of 1 M Fe^{3+} and 3 M SCN^{-} is higher than the energy of $Fe(SCN)_3$ (Figure 5d), with an energy difference of −2.165 Hartree. Typically, the reaction primarily releases energy in the form of thermal energy. Based on this, an infrared thermography camera was utilized to record the changes in thermal energy on microdroplet chemical reactors of oil-free MDCA surfaces and microdroplet chemical reactors of oil-loaded MDCA surfaces (Figure 5e). On the MDCA surface, the temperature at the center of the droplet was the lowest, with the ambient temperature surrounding the droplet being higher. As the chemical reaction progressed, the temperature at the droplet's center increased by 2.6 °C over 5 s and returned to normal after 10 s. In contrast, due to the encapsulation by the silicone oil layer, the baseline temperature of the droplet was approximately 6°C higher than that of the unencapsulated droplets, and the infrared thermography camera had a lower sensitivity to temperature changes the droplets on the SOMDCA surface compared to the droplets on the MDCA. The exothermic duration of the reaction lasted for 9 s, with an energy retention capacity approximately 1.8 times higher than that of the droplets without silicone oil encapsulation. In conclusion, the performance of SOMDCA in droplet fusion and reduction of energy loss within a confined environment holds significant potential across various fields. In chemical reaction engineering, it can optimize reaction conditions, minimize the occurrence of side reactions, and enhance product purity as well as experimental reproducibility. In the energy sector, it contributes to improving energy storage density and conversion efficiency. Within the realm of 3D printing and material synthesis, it ensures the uniformity and stability of materials post-fusion, thereby enhancing printing precision and material performance. In the food and cosmetics industry, droplet fusion and emulsification help maintain product stability and the efficacy of active ingredients. Furthermore, in the fields of dynamic displays and smart materials, it improves display quality and the responsiveness of materials. Finally, Table S2 shows the superiority of SOMDCA compared to other articles.

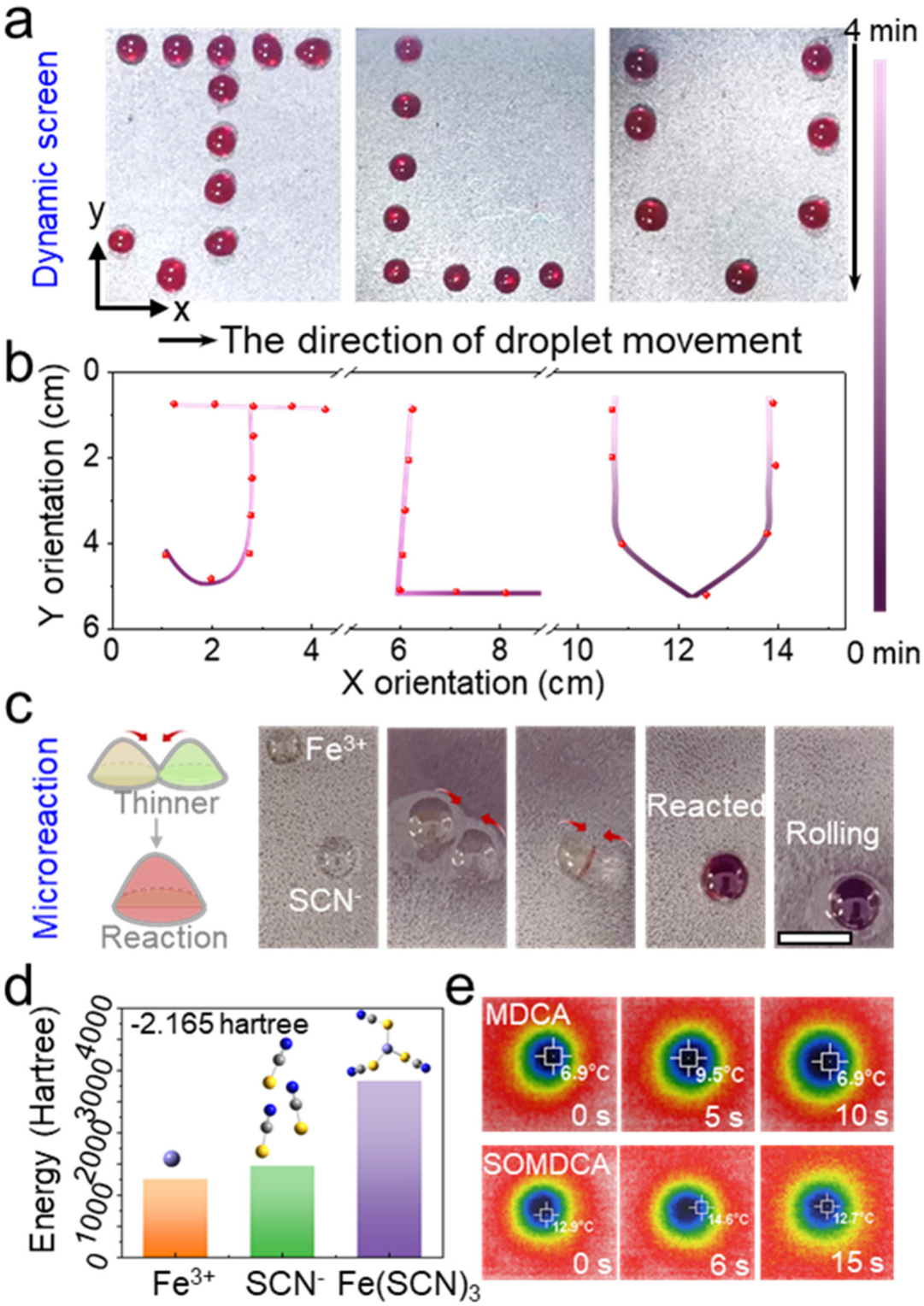

Figure 5. Dynamic screen and microreaction application of the SOMDCA. (**a**) SOMDCA manipulates the droplet for display instances. (**b**) SOMDCA manipulates the time profile of the droplets. (**c**) SOMDCA controls the droplet for microfluidic reactions. The interpolated scale bar is 1 cm. (**d**) Gauss 16 software simulates molecular energy maps. (**e**) Heat distribution diagram of chemical reaction with or without silicone oil coating.

3.6. Mechanism Analysis of Droplet Driven

The stable configuration of droplets on the surface of SOMDCA can be predicted through a thermodynamic framework: for the external interface (in an air environment), the oil spreads across the entire droplet as a thin covering layer, forming an oil-water interface, where $E_{oa} < E_{wa}$. For the internal interface (the droplet-substrate contact layer), a "wetting ridge" exists at the bottom of the droplet, where $E_{os} < E_{ws}$. The subscripts denote oil, air, water and substrate. The influence of structure on sliding behavior can be modelled by balancing gravitational

force and pinning force. When a droplet undergoes motion, its behavior can be characterized by the roll-off angle model. On a lubricant-infused surface, the roll-off angle is governed by the pinning force along the contact line, particularly influenced by contact angle hysteresis. The movement and rolling angle of the droplet are affected by the surface microstructure and the viscosity of the liquid. The equilibrium of forces at the point of tangency on the surface, which corresponds to the stable configuration of droplets on a surface wetted by a lubricant, is formulated based on the force balance principle: $\rho_w V g sin\alpha = R_b \Phi^{1/2}[\gamma_{ow}\,(cos\theta_{rec,os(w)} - cos\theta_{adv,os(w)}) + \gamma_{oa}\,(cos\theta_{rec,os(a)} - cos\theta_{adv,os(a)})]$, Where ρ_w is the liquid density, g is the gravitational acceleration, V is the droplet volume, R_b is the droplet base radius, $\Phi^{1/2}$ is the fraction of R_b, $\theta_{adv,ws(a)}$ and $\theta_{rec,ws(a)}$ are the advancing and receding contact angles of the droplet in air on the smooth solid surface, $\gamma_{oil-water}, \gamma_{oil-air}$ denote the oil-water and oil-air interfacial tensions, α represents the inclination angle of the substrate. In the presence of silicone oil, the triple contact line or the quadruple contact line does not exist, which is the reason why droplets can slide down with a low rolling angle even on MDCA surfaces with certain structures.

Furthermore, once the gravity of the droplet overcomes the pinning force, the droplet acquires a certain velocity to slide or roll off. For a droplet of volume it is anticipated that this velocity will depend on the contact line pinning and the viscosity of the lubricant. According to the research by J. David Smith et al. [40], $V^{2/3}\rho_w g/\gamma_{wa}(sin\alpha - sin\alpha^*)\,V^{1/3}/R_b = \mu_w v/\gamma_{wa}$, where μ_w is water dynamic viscosity, v is the steady-state shedding velocity, and R_b is the droplet base radius. This model suggests that the gravitational potential energy of the rolling droplet is primarily consumed in the viscous dissipation around the wetting ridge at the base of the droplet's slide. The thin layer covering the droplet has negligible inertial and gravitational forces. Therefore, the velocity is uniform along the streamline, and viscous dissipation can be ignored.

4. Conclusions

In summary, based on the principle that CIPs are magnetized and arranged in an orderly manner under the influence of a magnetic field, MDCA with strong subcompliance was developed in this paper. The Abbott curve simulation results of MDCA showed that the optimized MDCA had two types of heights of cilium array as well as excellent spatial distributability, which reduces the roughness of the cilia in a prostrated state and enhances the droplet slipperiness. Particularly, the presence of the micro-cilia increases the retention time of the silicone oil to a certain extent. In addition, under the drive of the programmable magnetic field, the droplets showed two states, upright and prostrated, which realized in situ fixation and actuation of the droplets, respectively. In order to further optimize the slippage performance of the droplets, the MDCA was surface modified with silicone oil. The SOMDCA can be not only used for precise manipulation of droplets on both spatial and temporal scales (S-trajectory transport, selective control, and velocity control of target droplets), but also provide a self-enclosed space for droplet fusion in chemical microreactions, thus enabling fine-tuning of reaction parameters and isolation from external contamination.

Supplementary Materials: The supporting information can be downloaded at: https://www.sciltp.com/journals/mi/2025/1/812/s1. References [41–47] are cited in Supplementary Materials.

Author Contributions: Z.Q. and Y.Z. designed the experiments. B.L., F.R. and Y.C. helped with sample pretreatment. Y.P., Z.Y., Y.C., F.R. and L.L. helped draw pictures. Z.Q., Y.Z. and B.L., wrote the manuscript. S.N., Z.H. and L.R. conceived the project. All authors have read and agreed to the published version of the manuscript.

Funding: This work was funded by the Foundation for Innovative Research Groups of the National Natural Science Foundation of China (No. 52021003), National Natural Science Foundation of China Excellent Youth Fund (No. 52222509), the National Natural Science Foundation of China (No. 52475300), Science and Technology Development Program of Jilin Province (No. SKL202402005), the Natural Science Foundation of Jilin Province (No. 20220101220JC), and "Fundamental Research Funds for the Central Universities".

Conflicts of Interest: The authors declare no conflict of interest.

References

1. Zhou, M.; Wu, Z.; Zhao, Y.; Yang, Q.; Huang, X. Droplets as Carriers for Flexible Electronic Devices. *Adv. Sci.* **2019**, *6*, 1901862. https://doi.org/10.1002/advs.201901862.
2. Li, J.; Han, X.; Li, W.; Yang, L.; Li, X.; Wang, L. Nature-Inspired Reentrant Surfaces. *Prog. Mater. Sci.* **2023**, *133*, 101064. https://doi.org/10.1016/j.pmatsci.2022.101064.
3. Sun, Q.; Wang, D.; Li, Y.; Zhang, J.; Ye, S.; Cui, J.; Chen, L.; Wang, Z.; Bütt, H.; Vollmer, D. Surface Charge Printing for Programmed Droplet Transport. *Nat. Mater.* **2019**, *18*, 936–941. https://doi.org/10.1038/s41563-019-0440-2.
4. Peng, W.; Lin, S.; Guan, D.; Chen, Y.; Wu, H.; Cao, L.; Huang, Y.; Li, F. Cactus-Inspired Photonic Crystal Chip for Attomolar Fluorescence Multi-analysis. *Anal. Chem.* **2023**, *95*, 2047–2053. https://doi.org/10.1021/acs.analchem.2c04729.

5. Hwang, Y.H.; Um, T.; Hong, J.; Ahn, G.N.; Qiao, J.; Kang, I.; Qi, L.; Lee, H.; Kim, D.P. Robust Production of Well-Controlled Microdroplets in a 3D-Printed Chimney-Shaped Milli-Fluidic Device. *Adv. Mater. Technol.* **2019**, *4*, 1900457. https://doi.org/10.1002/admt.201900457.
6. Plog, J.; Jiang, Y.; Pan, Y.; Yarin, A.L. Electrostatic Charging and Deflection of Droplets for Drop-on-Demand 3D Printing within Confinements. *Addit. Manuf.* **2020**, *36*, 101400. https://doi.org/10.1016/j.addma.2020.101400.
7. Zhang, Y.; Dong, Z.; Li, C.; Du, H.; Fang, N.; Wu, L.; Song, Y. Continuous 3D Printing from One Single Droplet. *Nat. Commun.* **2020**, *11*, 4685. https://doi.org/10.1038/s41467-020-18518-1.
8. Ma, S.; Liu, D.; Sheng, W.; Ma, Y.; Li, B.; Zhao, X.; Wang, X.; Zhou, F.; Liu, W. Bio-Inspired Wet/Lubricious/Adhesive Soft Matter and Performance Control in-between. *Adv. Bionics* **2024**, *1*, 29–56. https://doi.org/10.1016/j.abs.2024.09.002.
9. Zhang, S.; Chi, M.; Liu, T.; Luo, B.; Cai, C.; Wang, J.; Liu, Y.; Gao, C.; Wang, S.; Nie, S. Spontaneous Charging-induced Droplets Directional Steering. *Nano Energy* **2024**, *127*, 109766. https://doi.org/10.1016/j.nanoen.2024.109766.
10. Ferraro, D.; Serra, M.; Filippi, D.; Zago, L.; Guglielmin, E.; Pierno, M.; Descroix, S.; Viovy, J.-L.; Mistura, G. Controlling the Distance of Highly Confined Droplets in a Capillary by Interfacial Tension for Merging on-demand. *Lab Chip* **2019**, *19*, 136–146. https://doi.org/10.1039/c8lc01182f.
11. Zhang, X.; Sun, L.; Wang, Y.; Bian, F.; Wang, Y.; Zhao, Y. Multibioinspired Slippery Surfaces with Wettable Bump Arrays for Droplets Pumping. *Proc. Natl. Acad. Sci. USA* **2019**, *116*, 20863–20868. https://doi.org/10.1073/pnas.1912467116.
12. Li, G.; Zhang, Y.; Zhang, X.; Zhu, B.; Lei, Y.; Chen, D.; Shui, L.; Wu, G.; Xue, L. Filiform Papillae-Inspired Wearable Pressure Sensor with High Sensitivity and Wide Detection Range. *Adv. Funct. Mater.* **2024**, *35*, 2414465 https://doi.org/10.1002/adfm.202414465.
13. Wang, L.; Zhang, C.; Wei, Z.; Xin, Z. Bioinspired Fluoride-Free Magnetic Microcilia Arrays for Anti-Icing and Multidimensional Droplet Manipulation. *ACS Nano* **2023**, *18*, 526–538. https://doi.org/10.1021/acsnano.3c08368.
14. Gao, Z.; Lin, G.; Chen, Y.; Zheng, Y.; Sang, N.; Li, Y.; Chen, L.; Li, M. Moth-eye Manostructure PDMS Films for Reducing Reflection and Retaining Flexibility in Ultra-thin c-Si solar cells. *Sol. Energy* **2020**, *205*, 275–281. https://doi.org/10.1016/j.solener.2020.05.065.
15. Zhang, B.; Liao, X.; Chen, Y.; Xiao, H.; Ni, Y.; Chen, X. Rapid Programmable Nanodroplet Motion on a Strain-Gradient Surface. *Langmuir* **2019**, *35*, 2865–2870. https://doi.org/10.1021/acs.langmuir.8b03774.
16. Tian, L.; Dou, H.; Shao, Y.; Yi, Y.; Fu, X.; Zhao, J.; Fan, Y.; Ming, W.; Ren, L. Magnetically Controlled Super-wetting Surface Switching between Ultra-low and Ultra-high Droplet Adhesion. *Chem. Eng. J.* **2023**, *456*, 141093. https://doi.org/10.1016/j.cej.2022.141093.
17. Shao, K.; Jiang, S.; Hu, Y.; Zhang, Y.; Li, C.; Zhang, Y.; Li, J.; Wu, D.; Chu, J. Bioinspired Lubricated Slippery Magnetic Responsive Microplate Array for High Performance Multi-Substance Transport. *Adv. Funct. Mater.* **2022**, *32*, 2205831. https://doi.org/10.1002/adfm.202205831.
18. Ko, J.; Zhao, Z.; Hwang, S.H.; Kang, H.; Ahn, J.; Jeon, S.; Bok, M.; Jeong, Y.; Kang, K.; Cho, I.; et al. Nanotransfer Printing on Textile Substrate with Water-Soluble Polymer Nanotemplate. *ACS Nano* **2020**, *14*, 2191–2201. https://doi.org/ 10.1021/acsnano.9b09082.
19. Song, Y.; Yang, J.; Zhang, X.; Zhang, Z.; Hu, X.; Cheng, G.; Liu, Y.; Lv, G.; Ding, J. Temperature-Responsive Peristome-Structured Smart Surface for the Unidirectional Controllable Motion of Large Droplets. *Microsyst. Nanoeng.* **2023**, *9*, 119. https://doi.org/10.1038/s41378-023-00573-5.
20. Rao, Q.; Tong, Z.; Song, L.; Ali, A.; Hou, Y.; He, Q.; Lu, J.; Gao, X.; Zhan, X.; Zhang, Q. NIR-driven Fast Construction of Patterned-Wettability on Slippery Lubricant Infused Surface for Droplet Manipulation. *Chem. Eng. J.* **2022**, *428*, 131141. https://doi.org/10.1016/j.cej.2021.131141.
21. Liang, X.; Karnaukh, K.; Zhao, L.; Seshadri, S.; DuBose, A.; Bailey, S.; Cao, Q.; Cooper, M.; Xu, H.; Haggmark, M.; et al. Dynamic Manipulation of Droplets on Liquid-Infused Surfaces Using Photoresponsive Surfactant. *Acs Cent. Sci.* **2024**, *10*, 684–694. https://doi.org/10.1021/acscentsci.3c00982.
22. Zhang, Q.; Bai, X.; Li, Y.; Zhang, X.; Tian, D.; Jiang, L. Ultrastable Super-Hydrophobic Surface with an Ordered Scaly Structure for Decompression and Guiding Liquid Manipulation. *ACS Nano* **2022**, *16*, 16843–16852. https://doi.org/10.1021/acsnano.2c06749.
23. Huo, X.; Li, L.; Yang, Y.; Liu, X.; Yu, Q.; Wang, Q. The Dynamics of Directional Transport of a Droplet in Programmable Electrowetting Channel. *Phys. Fluids* **2023**, *35*, 032105. https://doi.org/10.1063/5.0139965.
24. Li, N.; Yang, P.; Bai, Z.; Shen, T.; Liu, Z.; Qin, S.; Hu, J.; Yu, C.; Dong, Z.; Chen, X. Bioinspired Electrostatic Capture-and-Release System for Precise Microdroplet Manipulation. *Adv. Mater.* **2025**, *37*, 2418711. https://doi.org/10.1002/adma.202418711.
25. Kravanja, G.; Kriegl, R.; Hribar, L.; Glavan, G.; Drevensek-Olenik, I.; Shamonin, M.; Jezersek, M. Magnetically Actuated Surface Microstructures for Efficient Transport and Tunable Separation of Droplets and Solids. *Adv. Eng. Mater.* **2023**, *25*, 2301000. https://doi.org/ 10.1002/adem.202301000.
26. Chi, Y.; Evans, E.; Clary, M.R.; Qi, F.; Sun, H.; Cantu, S.N.; Capodanno, C.M.; Tracy, J.; Yin, J. Magnetic Kirigami

Dome Metasheet with High Deformability and Stiffness for Adaptive Dynamic Shape-Shifting and Multimodal Manipulation. *Sci. Adv.* **2024** *10*, eadr8421. https://doi.org/10.1126/sciadv.adr8421.

27. Wang, W.; Timonen, J.; Carlson, A.; Drotlef, D.; Zhang, C.; Kolle, S.; Grinthal, A.; Wong, T.S.; Hatton, B.; Kang, S.H.; et al. Multifunctional Ferrofluid-Infused Surfaces with Reconfigurable Multiscale Topography. *Nature* **2018**, *559*, 77–82. https://doi.org/10.1038/s41586-018-0250-8.
28. Han, K.; Snezhko, A. Programmable Chiral States in Flocks of Active Magnetic Rollers. *Lab Chip* **2021**, *21*, 215–222. https://doi.org/10.1039/d0lc00892c.
29. Park, S.; Choi, G.; Kang, M.; Kim, W.; Kim, J.; Jeong, H.E. Bioinspired Magnetic Cilia: From Materials to Applications. *Microsyst. Nanoeng.* **2023**, *9*, 153. https://doi.org/10.1038/s41378-023-00611-2.
30. Yang, C.; Wu, L.; Li, G. Magnetically Responsive Superhydrophobic Surface: In Situ Reversible Switching of Water Droplet Wettability and Adhesion for Droplet Manipulation. *ACS Appl. Mater. Interfaces* **2018**, *10*, 20150–20158. https://doi.org/10.1021/acsami.8b04190.
31. Kim, J.; Kang, S.; Lee, B.; Ko, H.; Bae, W.; Suh, K.; Kwak, M.; Jeong, H. Remote Manipulation of Droplets on a Flexible Magnetically Responsive Film. *Sci. Rep.* **2015**, *5*, 17843. https://doi.org/10.1038/srep17843.
32. Chen, Y.; Quan, Z.; Xie, H.; Li, B.; Zhao, J.; Niu, S.; Han, Z.; Ren, L. Bioinspired Active Dynamic Dust Remover for Multiscale Stardust Repelling of Unmanned Probe Surface. *Nano Lett.* **2024**, *25*, 553–561. https://doi.org/10.1021/acs.nanolett.4c05480.
33. Lu, G.; Cui, H.; Zhao, T.; Yang, W.; Wang, M.; Liu, Z.; Niu, S.; Ren, L. Cilia-Inspired Functional Channels for High-Speed and Directional PEMFC Drainage. *Adv. Funct. Mater.* **2024**, *35*, 2416005. https://doi.org/10.1002/adfm.202416005.
34. Zhang, X.; Ben, S.; Zhao, Z.; Ning, Y.; Li, Q.; Long, Z.; Yu, C.; Liu, K.; Jiang, L. Lossless and Directional Transport of Droplets on Multi-bioinspired Superwetting V-shape Rails. *Adv. Funct. Mater.* **2023**, *33*, 2212217. https://doi.org/10.1002/adfm.202212217.
35. Feng, S.; Zhu, P.; Zheng, H.; Zhan, H.; Chen, C.; Li, J.; Wang, L.; Yao, X.; Liu, Y.; Wang, Z. Three-Dimensional Capillary Ratchet-Induced Liquid Directional Steering. *Science* **2021,** *373*, 1344–1348. https://doi.org/10.1126/science.abg7552.
36. Li, Y.; Liu, X.; Wang, R.; Jiao, S.; Liu, Y.; Lai, H.; Cheng, Z. Triple-Bioinspired Shape Memory Microcavities with Strong and Switchable Adhesion. *ACS Nano* **2023**, *17*, 23595–23607. https://doi.org/10.1021/acsnano.3c06651.
37. Li, Y.; Wang, R.; Jiao, S.; Lai, H.; Liu, Y.; Cheng, Z. Beetle-Inspired Oil-Loaded Shape Memory Micro-Arrays with Switchable Adhesion to Both Solid and Liquid. *Chem. Eng. J.* **2023**, *461*, 141927. https://doi.org/10.1016/j.cej.2023.141927.
38. Hev, Z.; Mu, L.; Wang, N.; Su, J.; Wang, Z.; Luo, M.; Zhang, C.; Li, G.; Lan, X. Design, Fabrication, and Applications of Bioinspired Slippery Surfaces. *Adv. Colloid Interface* **2023**, *318*, 102948. https://doi.org/10.1016/j.cis.2023.102948.
39. Yue, T.; Bloomfield-Gadêlha, H.; Rossiter, J. Snail-Inspired Water-Enhanced Soft Sliding Suction for Climbing Robots. *Nat. Commun.* **2024**, *15*, 4038. https://doi.org/10.1038/s41467-024-48293-2.
40. Smith, J.; Dhiman, R.; Anand, S.; Reza-Garduno, E.; Cohen, R.; McKinley, G.; Varanasi, K. Droplet Mobility on Lubricant-Impregnated Surfaces. *Soft Matter* **2013**, *9*, 1772–1780. https://doi.org/10.1039/c2sm27032c.
41. Manabe, K.; Saito, K.; Nakano, M.; Ohzono, T.; Norikane, Y. Light-Driven Liquid Conveyors: Manipulating Liquid Mobility and Transporting Solids on Demand. *ACS Nano* **2022**, *16*, 16353–16362. https://doi.org/10.1021/acsnano.2c05524.
42. Wang, Z.; Xu, Q.; Wang, L.; Heng, L.; Jiang, L. Temperature-induced switchable interfacial interactions on slippery surfaces for controllable liquid manipulation. *J. Mater. Chem. A* **2019**, *7*, 18510–18518. https://doi.org/10.1039/c9ta05164c.
43. Ichimura, K.; Oh, S.; Nakagawa, M. Light-Driven Motion of Liquids on a Photoresponsive Surface. *Science* **2000**, *288*, 1624–1626. https://doi.org/10.1126/science.288.5471.1624.
44. Hwang, H.; Papadopoulos, P.; Fujii, S.; Wooh, S. Driving Droplets on Liquid Repellent Surfaces via Light-Driven Marangoni Propulsion. *Adv. Funct. Mater.* **2022**, *32*, 2111311. https://doi.org/10.1002/adfm.202111311.
45. Tang, B.; Meng, C.; Zhuang, L.; Groenewold, J.; Qian, Y.; Sun, Z.; Liu, X.; Gao, J.; Zhou, G. Field-Induced Wettability Gradients for No-Loss Transport of Oil Droplets on Slippery Surfaces. *ACS Appl. Mater. Interfaces* **2020**, *12*, 38723–38729. https://doi.org/10.1021/acsami.0c06389.
46. Chen, C.; Huan, Z.; Jiao, Y.; Shi, L.; Zhang, Y.; Li, J.; Li, C.; Lv, X.; Wu, S.; Hu, Y. In Situ Reversible Control between Sliding and Pinning for Diverse Liquids under Ultra-Low Voltage. *ACS Nano* **2019**, *13*, 5742–5752. https://doi.org/10.1021/acsnano.9b01180.
47. Feng, S.; Hou, Y.; Zheng, Y. Programmable Curvilinear Self-Propelling of Droplets without Preset Channels. *Droplet* **2025**, *3*, e138. https://doi.org/10.1002/dro2.138.